

Learning Spatial Relationships between Samples of Patent Image Shapes

Juan Castorena, Manish Bhattarai and Diane Oyen *

Abstract

Binary image based classification and retrieval of documents of an intellectual nature is a very challenging problem. Variations in the binary image generation mechanisms which are subject to the document artisan designer including drawing style, view-point, inclusion of multiple image components are plausible causes for increasing the complexity of the problem. In this work, we propose a method suitable to binary images which bridges some of the successes of deep learning (DL) to alleviate the problems introduced by the aforementioned variations. The method consists on extracting the shape of interest from the binary image and applying a non-Euclidean geometric neural-net architecture to learn the local and global spatial relationships of the shape. Empirical results show that our method is in some sense invariant to the image generation mechanism variations and achieves results outperforming existing methods in a patent image dataset benchmark.

1. Introduction

Classification and retrieval of documents of intellectual nature is an important and challenging problem. Most widely used methods rely mainly on text and perform the aforementioned tasks by comparing document relevance to text queries. However, intellectual documents typically include and convey valuable information not only through text but also through figures or illustrations. In fact, the USPTO includes in their guidelines for patent application design that "the drawing disclosure is the most important element of the application" [1]. Effective methods which exploit such visual information could thus further improve and facilitate the classification, retrieval and search of such documents of intellectual domain. Unfortunately, image based classification/retrieval from intellectual content (e.g., patents, research papers) still remains a very challenging problem.

Problems affecting effective image based classification and retrieval of documents of intellectual content are plausibly the image generation mechanisms. These generally include the highly subjective drawing style of the artisan, its preferred view-point to highlight aspects of relevance, the inclusion of multiple objects or components in some sense related and whose spatial distribution may or may not be of importance and the lack of image texture and color. Note here that view-point includes a projection of a 3D rotation and translation into the image reference frame which induces a scaling factor while style includes binary (black and white) images of varying line thickness, dashed/dotted lines and shadings.

A number of methods and challenges have been envisioned as attempts to resolve the image based classification/retrieval problem for patent related applications. For example, the work in [2] focuses on retrieval by ranking a Euclidean distance similarity based on the distribution of radial and angular

*J. Castorena, M. Bhattarai and D. Oyen are with the Los Alamos National Laboratory, Los Alamos, NM, 87545 USA
e-mail: {jcastorena, ceodsppectrum, doyen}@lanl.gov



Figure 1: Image shape analysis system. Shape and background in an image are segmented in the shape extraction block, the shape is then sparsely sampled in the sampling block while the learn shapes block learns features characterizing the spatial relationships between the point samples of the shape.

features from image contours. The adaptive hierarchical density histogram (AHDH) method of [3] consists of an adaptive multi-resolution-multi feature representation with features from black and white pixel counts across the multi-resolution blocks. [4] fused a set of local handcrafted features including local binary patterns and edge histograms to train a linear SVM. The last relevant work achieving the highest accuracy is the work of [5]. This method, constructed Fisher vectors (FV) through the parametric estimation of a Gaussian mixture model (GMM) representation of the distribution of local SIFT features computed across the entire image. Distinct classifiers were trained with SVM significantly outperforming the others. Unfortunately, most of these methods suffer in performance achieving classification accuracies around 65% with the exception of [5] with 90%.

Convolutional neural networks (CNN's) [6] within deep learning (DL) have revolutionized the way by which we do image analysis and have outperformed traditional methods in many application problems [7]. Connecting such research advances to solve the problems being faced for the classification/retrieval of images of intellectual property would be highly beneficial. However, application of off-the-shelf CNN architectures operating in the Euclidean image domain although straightforward are not the most efficient and do not exploit the full potential of CNN's for this specific problem mainly because binary images are texture-less. But secondly, because of their inability to cope with the generation mechanisms causing variations in the absence of sufficient data characterizing all potential combinations of these [8]. This later, i.e., controlling and intervening the highly subjective nature of the generation process of intellectual images as well as its access to generate a sufficient dataset is extremely challenging.

Here, we propose a learning based method that aims both at making the application of neural-nets on binary images more efficient and at disentangling the learned functionals from some of the variations in the image generation mechanisms. Efficient application of the neural net is made by operating directly on the object or shape of interest contained and extracted from the patent image rather than on the entire image. This of-course implies usage of a neural-net operating on the non-Euclidean domain learning local and global features characterizing the spatial relationships of the shape. Operating on the shape allows one to disentangle from the generation mechanisms of scaling, translation by centering and normalizing while plausibly introducing some invariance to rotations and style from the learned local and global features characterizing spatial relationships. Given this, our paper presents the proposed approach in Section 2. Section 3 presents experimental results comparing classification/retrieval performance across different datasets with scaling, rotation and translation transformations, and finally Section 4 concludes our findings.

2. Approach

The basis of the method we propose consists on the extraction of shapes from images, point sampling from the shape and finally learning node and edge interconnection features that characterize shape point samples. A summary of the system is shown in Figure 1.

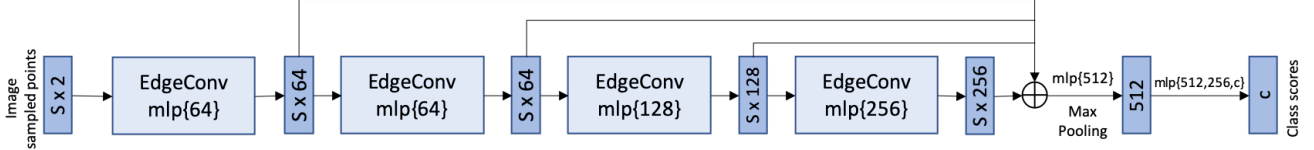


Figure 2: Dynamic Graph CNN Architecture.

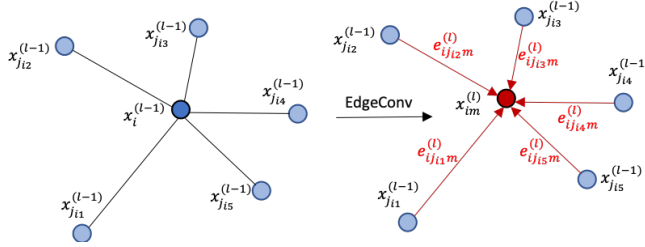


Figure 3: EdgeConv at a node.

2.1. Point clouds from image shapes

Shapes are first extracted from images by segmenting shape from background through the well known adaptive thresholding method of Otsu [9]. Note that the use of a shape segmentation method is a necessity only in cases when images are non-binary. Such an extraction and analysis on the non-Euclidean spatial composition of a shape instead of the Euclidean analysis on image pixel values will enable the learning engine to be invariant against image texture or color; a property of crucial importance to many applications.

Following, a representative sparse point-cloud of the shape is extracted by clustering the pixel locations conforming the segmented shape. The algorithm we use here for such clustering is the mini-batch k -means [10] which is orders of magnitude more computationally efficient than standard k -means with only small penalties in performance. The efficiency of such method is obtained by processing data iteratively in batches of randomly picked points with centroids computed through stochastic gradient descent (SGD). Each of the estimated S centroids denoted here by $\mathbf{x}_i^{(0)} \in \mathbb{R}^2$ for $i \in \{1, \dots, S\}$ contains the corresponding (x, y) location of the estimates. Comforming all of the k -means centroids results in a point cloud $\mathbf{X}^{(0)} = \{\mathbf{x}_1^{(0)}, \dots, \mathbf{x}_S^{(0)}\}$ of sparsely sampled representative points of the shape. Note that, throughout this paper the superscript (0) denotes an input.

Shape sampling is solely meant here to reduce the computational complexity of the learning algorithm described in the next section, specially in cases when the shape is not complex. However, dense point clouds including all the (x, y) pixel locations conforming a shape could also be used instead. This of course at the cost of higher computational complexity imposed on the learning algorithm.

2.2. Learning shapes through graphs

The sampled points $\mathbf{X}^{(0)}$ of the shape are used as input to a deep neural net that learns features characterizing the meaningful spatial relationships between the points. Here, the sampled points and their spatial relationships are represented as nodes and edges of a graph, respectively. The learning engine of such graphs is a dynamic graph CNN (DGCNN) [11] architecture dynamically operating and learning graphs across its layers. Here, each layer l produces graphs $\mathcal{G}_m^{(l)} = (\mathcal{V}^{(l)}, \mathcal{E}_m^{(l)})$ indexed by $m \in \{1, \dots, M^{(l)}\}$ by dynamically associating k nearest learned feature neighbors (f- k NN's) according to node distances

in the feature space. An instance of the DGCNN architecture we use is shown in Figure 2. Such an architecture consists of a sequence of $M^{(l)}$ -dim edgeConv layers consisting each of node and edge connection features $\mathbf{x}_i^{(l)} \in \mathbb{R}^{M^{(l)}}$ for $i \in \mathcal{V}^{(l)}$ and $\mathbf{e}_{ij}^{(l)} \in \mathbb{R}^{M^{(l)}}$ for $(i, j) \in \mathcal{E}_m^{(l)}$, respectively. Node features $x_{im}^{(l)}$ are computed element-wise as

$$x_{im}^{(l)} = \max_{j:(i,j) \in \mathcal{E}_m^{(l)}} e_{ijm}^{(l)} \quad (1)$$

where the maximum is computed over the f - k NN’s at the node i and edge features computed element-wise as

$$e_{ijm}^{(l)} = \text{ReLU}(\boldsymbol{\theta}_m^{(l)} \cdot (\mathbf{x}_j^{(l-1)} - \mathbf{x}_i^{(l-1)}) + \boldsymbol{\phi}_m^{(l)} \cdot \mathbf{x}_i^{(l-1)}) \quad (2)$$

with $\boldsymbol{\theta}_m^{(l)}, \boldsymbol{\phi}_m^{(l)} \in \mathbb{R}^{M^{(l)}}$ being parameters of the learned convolution filters. Note that the first inner product in Eq (2) captures local information whereas the second inner product captures global information. Fig. 3 illustrates the mechanism by which the edgeConv layer generates features in a node. First it computes the f - k NNs j_{i_1}, \dots, j_{i_5} centered at node i using Euclidean distances between features. Then, computes functions e'_{ijm} in Eq. (2) through the learned filters only for the f - k NNs and then applies (1). Implementations of these operators can be framed as a shared multi-layer perceptron (mlp).

3. Experiments

Evaluation of the proposed approach is tested against the task of classification of the MNIST benchmark [6] and the CLEF-IP dataset of patent images in [12]. The intent to include experiments on the MNIST dataset is to demonstrate the inability of standard CNN’s operating in the Euclidean domain to cope with data transformations in the absence of sufficient data characterizing these. A matter of crucial importance to build effective classification/retrieval solutions in the patent application realm.

3.1. Point cloud extraction

We generate a point-cloud for each image shape in the aforementioned datasets following Section 2.1. Figure 4 illustrates a few representative point cloud examples where the first row shows the MNIST digit images and the second row represents the corresponding extracted point clouds. The point-clouds are each of size 10×2 (i.e., $S = 10$) for which case the mini-batched k -means algorithm runs near real-time and thus does not represent a significant computational bottleneck. Here, we also observe



Figure 4: Sampling points from MNIST digit images. Row 1: MNIST images, Row 2: Sampled points.

that the proposed sampling mechanism captures the underlying structure of the MNIST shapes even when $S = 10$. For illustration purposes we also include in Figure 5 an example that shows the effect of increasing sparsity. Note that at the sparsest point cloud it is visually difficult to identify the digit and some ambiguity exists as to whether it is a 2, 3 or an 8. Fortunately, with sparsity of at least $S = 10$ the digit can be identified. Such effect is consistent with at least a vast number of examples manually inspected from the MNIST.

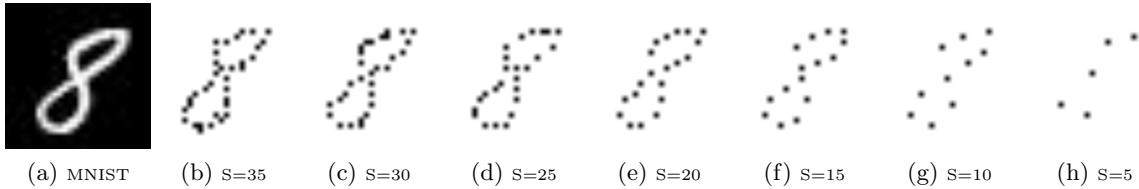


Figure 5: MNIST digit point cloud as a function of sparsity

In addition, we also include representative examples of the sampled shapes extracted from CLEF-IP’s [12] images extracted from patent documents. Figs. 6(a-c) are the raw images while Figs. 6(d-f) are the results of sparsely sampling the corresponding image shapes in (a-c) with $S = 1000$. Note that the sampling mechanism we employ visually preserves the shapes in all three cases as long as the point-cloud is relatively dense.

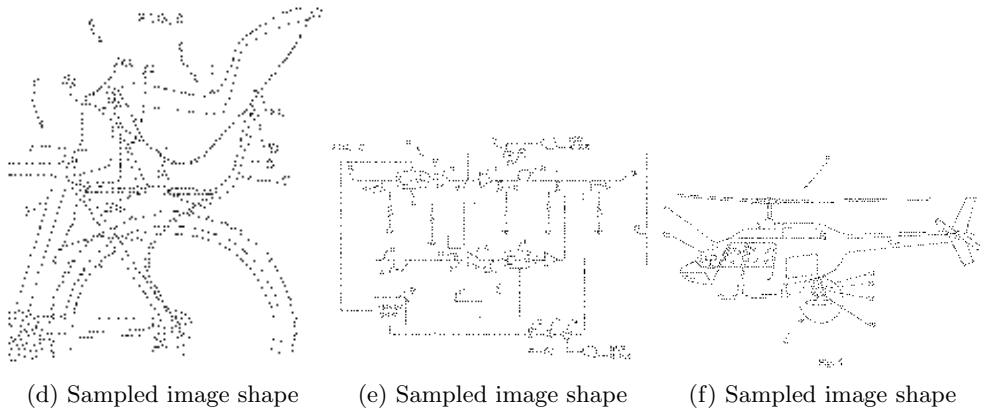
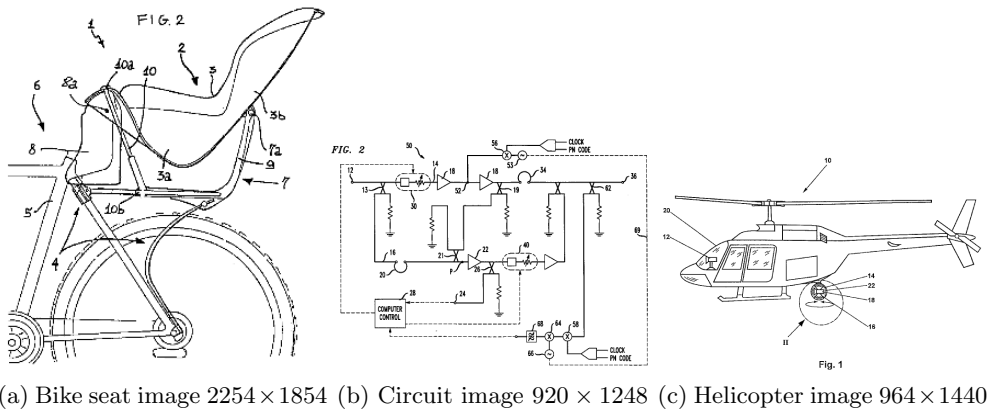


Figure 6: Sparse sampling of CLEF-IP image shapes.

3.2. Classification

Following the architecture model of [11] we use four EdgeConv layers as shown in Figure 2 of which the first three are fully-connected producing, respectively, features of size (64, 64, 128, 256). Max/sum pooling is used, unless otherwise specified the number of f- k NN is set to 5, dropout with keep probability of 0.5 and all layers include LeakyReLU and batch normalization.

For training, we use stochastic gradient descent (SGD) with self-adaptive learning rate. The rule to self-adapt is based on the warm restart method of [13] with an initial value of 0.1. Batch size is set to 32, momentum for batch normalization is set to 0.9 and #epochs = 100. We tested performance with a variety of number of parameters and the ones selected are the ones that yielded the best results.

Shapes are extracted from the image datasets by first transforming them into binary images through segmentation with Otsu’s adaptive thresholding method [9]. After the shape-background segmentation, each shape is sampled following the method description in Section 2.1. A point cloud of size $S \times 2$ is obtained for each 28×28 image that is subsequently centered and normalized to be within the unit ℓ_2 -norm ball.

The first experiment is intended to obtain MNIST classification performance against the sparsity of the point cloud extracted from the image shapes. This, to justify sampling a shape sparsely with higher computational complexity benefits over denser points clouds. For this experiment, partitions of 42K and 28K images were utilized to train and test, correspondingly. Figure 7 illustrates classification performance as a function of point cloud sparsity. Our results validate the intuition that classification performance does not suffer with sparser point-clouds above a certain level; in this case $S > 15$. At sparsity $S = 5$ the shape is no longer visually identifiable from other sampled shapes as observed in Figure 5.h.

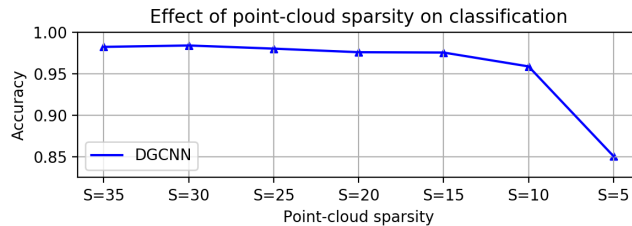


Figure 7: Classification versus point cloud sparsity.

A comparison of MNIST classification performance against a CNN method as training dataset size is varied was also conducted with results included in Fig. 8. This with the intent to observe the capabilities of the neural-net to learn features effectively when dataset size is reduced significantly. The methods we compared against are the LeNet-5 [6] with full 28×28 image inputs and the DGCNN architecture. Note that the LeNet-5 network can be considered as one of the smallest sized neural-nets out there thus being one of the least data hungry architectures which is of high appeal for our application. When comparing against LeNet-5, our findings show that the DGCNN performs consistently with variations in dataset size even better than the LeNet-5 in the lower size extreme case.

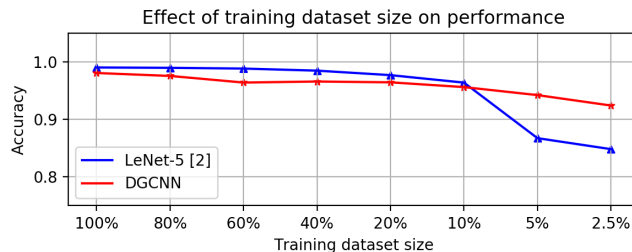


Figure 8: Classification versus training dataset size.

Evaluations on classification were performed now against the effect of data transformations that can plausibly influence the patent image generation mechanisms. Two experimental cases are included with

the transformed test data: (1) when training examples include images subjected to the corresponding transformations and (2) when training does not include examples of the transformed data. Since the MNIST dataset is the simplest to manipulate for transformations we use it as our comparison benchmark. The transformations for which we test here are random uniformly sampled from the limit $\pm 90^\circ$ for rotations, ± 9 pixels for translations in both horizontal and vertical directions and scaling in the (0.2,1) level. Table 1 summarizes the comparison results of performance against such transformations. Here, the results at the same row as the transformation label (e.g., "scale") show performance in the case of (2) i.e., when training data does not include transformation examples. The row where the "w re-training" label is (right under the transformation label) corresponds to performance of (1) when transformation examples of the expected transformation levels are included in the training data. These results show

Table 1: Classification against transformations on the MNIST dataset.

Transformation	LeNet-5 [6]	Proposed
scale	0.630	0.985
w re-training	0.961	
rotation	0.562	0.933
w re-training	0.981	
translation	0.286	0.995
w re-training	0.976	
scale, rot translate	0.134	0.935
w re-training	0.874	
binary inversion	0.257	0.992
w re-training	0.991	

that our proposed framework remains more or less invariant to the aforementioned transformations in comparison to LeNet-5 and that it outperforms it in most cases in its own intended benchmark dataset. The centering and ℓ_2 normalization of point clouds from extracted shapes makes our method invariant to scaling and translation transformations while some invariance to rotations is learned by the neural net exploiting spatial relationships between sampled points. In general, we can say that analysis of shapes extracted from images with the proposed method better copes to rigid body transformations in the 2D plane and across scales. However, this is not necessarily true for general view-point 3D-2D projections as these may include overlapping but potentially different information depending on the view-point drawing mechanism. The result in the binary inversion case was interesting, it showed that LeNet-5 suffered when the background was negatively correlated with the expected shape pixel level, a performance degradation issue mentioned in [14].

The final experiment on classification evaluates the proposed method against the CLEF-IP [12] patent image dataset. This dataset was built as a classification challenge including image categorization into one of the 9 classes: drawing, flowchart, graph, symbol, math, table, program, chem, geneseq. A representative example of the images for each of these classes is shown in Figure 9. Note that CLEF-IP dataset contains image shapes from an unknown and varying viewpoint. Such viewpoints are assumed here to be a projection of a rigid body transformation (3D rotation and translation) into the 2D image space. Although such viewpoints and generation process of patent figures are decided at the best discretion

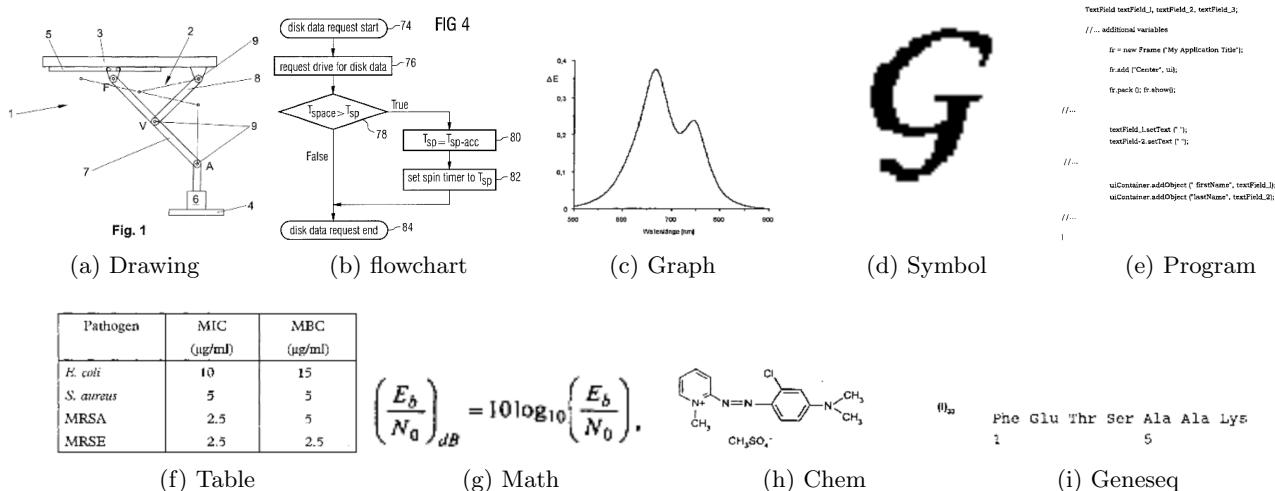


Figure 9: Examples of the CLEF-IP 9-class images.

of the patent artist to highlight certain aspects of the inventions, we assume here that this mechanism is random and that we have no intervention power on its generation. In addition, some figures contain multiple cross-class components which represents more challenges for learning class characteristics. Figure 10 illustrates examples of some of these variations together with an example presenting multiple components in a patent image.

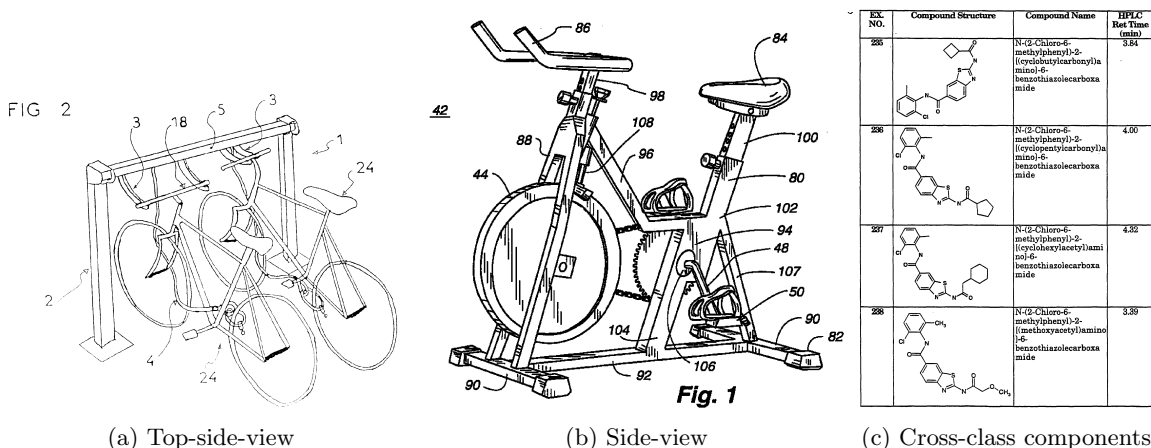


Figure 10: Variations of CLEF-IP patent figures.

The CLEF-IP dataset contains approximately 38K unbalanced-class images partitioned into the training and testing subsets. Each image was sampled and used as input to a DGCNN to learn the spatial relationships characterizing the shape classes. The sparsity of sampling was set in this case to $S = 1000$ and the f - k NN was set to 25. Intuition behind the usage of such sparsity is that in general the CLEF-IP contains images of significantly higher complexity compared to the simpler MNIST shapes. To learn the spatial relationships between the shape samples, the hyperparameters of the DGCNN were set to be the

same as those described at the beginning of this section. For comparison, we also include classification performance against two standard CNN methods: the basic LeNet-5 and the more sophisticated residual image learning ResNet-50 architecture [15]. In addition, we include results from [5] whose method was specifically designed for patent image based classification and whose performance is the best for this task, to the best of our knowledge. The results we obtained were summarized in table 2.

Table 2: Classification performance on CLEF-IP [12]

LeNet-5 [6]	Resnet-50 [15]	FV + SVM [5]	Proposed
0.555	0.244	0.907	0.942

Empirical results reflect that CNN’s operating in the Euclidean domain are not powerful enough to disentangle performance from view-point, drawing style and the presence of multiple components in binary patent imagery. The method of [5] based on the Fisher vector representation performs nicely and better than the standard CNN methods for this task. However, our proposed method seems to better cope with the plausible variations in the image generation mechanism and outperforms all compared methods which includes to the best of our knowledge the best so far for the specific task.

3.3. Retrieval

In addition to the classification task we also compare the performance of the proposed approach against the standard structural similarity Index (SSIM) method [16] in a retrieval task. We tested against the MNIST, fashion-MNIST [17] and CLEF-IP datasets described in the previous subsection and show that the proposed framework performs significantly better than the SSIM approach. To measure performance, we use the mean average precision (MAP) overall retrievals computed as:

$$\text{MAP} = \frac{\sum_{q=1}^Q \text{Ave}(P(q))}{Q} \tag{3}$$

where Q is the number of queries and $\text{Ave}(P(q))$ is the precision average of score for each query q . Here, $\text{Ave}(P(q))$ is obtained by computing the average number of items correctly retrieved in a k nearest neighborhood.

In the case of the proposed method, we re-use the concatenated local and global features learned in the classification task after the fourth EdgeConv layer in Figure 2. For illustrative purposes we show how the learned features naturally cluster for the CLEF-IP dataset by using the t-Distributed Stochastic Neighbor Embedding(t-SNE) [18] projection. Note in Figure 11 that features are nicely packed which seem as promising to be used to effectively retrieve similar shapes. Standard SSIM computes the structural pairwise similarity between all the image combinations in the test dataset partition and yields the set of k -images with the highest similarity measure given a query. With that, we summarize the MAP scores in both Figure 12 and in Table 3 for quantitative clarity. Here, we note that the proposed method for this task outperforms SSIM in most cases, except on the MNIST dataset where there is a huge structural uniformity in similarity within class samples without significant view-point variations.

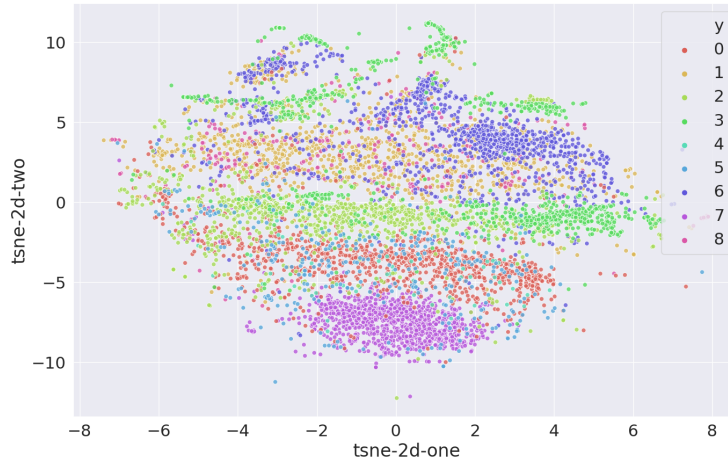


Figure 11: TSNE projection of the features extracted for CLEF-IP test dataset at the embedding layer of DGCNN.

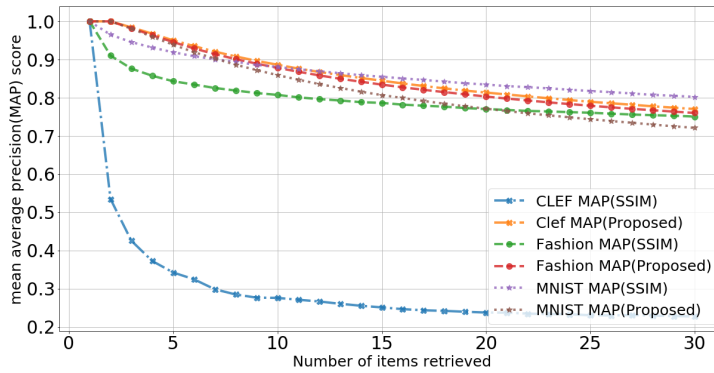


Figure 12: Mean average precision (MAP) analysis for different datasets using SSIM vs proposed approach.

Table 3: Retrieval Performances.

Dataset	MAP	MAP	MAP
	@10 retrievals	@20 retrievals	@30 retrievals
MNIST	0.88(SSIM)	0.83(SSIM)	0.80(SSIM)
	0.86(DGCNN)	0.77(DGCNN)	0.72(DGCNN)
fashion-MNIST	0.807(SSIM)	0.770(SSIM)	0.750(SSIM)
	0.878(DGCNN)	0.803(DGCNN)	0.760(DGCNN)
CLEF-IP	0.276(SSIM)	0.238(SSIM)	0.227(SSIM)
	0.886(DGCNN)	0.814(DGCNN)	0.771(DGCNN)

4. Conclusion

In this work, we proposed a method connecting the successes of deep learning (DL) to alleviate some of the problems being faced in patent image classification/retrieval applications. The method combines a shape extraction pre-processing stage with a neural net operating on the spatial representation of the shape (i.e., in the non-Euclidean domain). Empirical results demonstrate the ability of the proposed method to better cope with the plausible binary image generation mechanisms which are of a highly subjective nature in patent documents. Such mechanisms included variations in drawing style, view-point, and presence of multiple components or image parts.

Acknowledgement

Research was supported by the Laboratory Directed Research and Development program of Los Alamos National Laboratory under project number LDRD-20200041ER.

References

- [1] United States Patent and Trademark Office (USPTO), “Design patent application guide,” <https://www.uspto.gov/patents-getting-started/patent-basics/types-patent-applications/design-patent-application-guide>.
- [2] Z. Zhiyuan, Z. Juan, and X. Bin, “An outward-appearance patent-image retrieval approach based on the contour-description matrix,” in *2007 Japan-China Joint Workshop on Frontier of Computer Science and Technology (FCST 2007)*, 2007, pp. 86–89.
- [3] Panagiotis Sidiropoulos, Stefanos Vrochidis, and Ioannis Kompatsiaris, “Content-based binary image retrieval using the adaptive hierarchical density histogram,” *Pattern Recognition*, vol. 44, no. 4, pp. 739 – 750, 2011.
- [4] Roland Mörzinger, Andras Horti, Georg Thallinger, Naeem Bhatti, and Allan Hanbury, “Classifying patent images.,” in *CLEF (Notebook Papers/Labs/Workshop)*. Citeseer, 2011.
- [5] Gabriela Csurka, Jean-Michel Renders, and Guillaume Jacquet, “Xrce’s participation at patent image classification and image-based patent retrieval tasks of the clef-ip 2011,” 09 2011.
- [6] Y. Lecun, L. Bottou, Y. Bengio, and P. Haffner, “Gradient-based learning applied to document recognition,” *Proceedings of the IEEE*, vol. 86, no. 11, pp. 2278–2324, Nov 1998.
- [7] Yann LeCun, Y Bengio, and Geoffrey Hinton, “Deep learning,” *Nature*, vol. 521, pp. 436–44, 05 2015.
- [8] Giambattista Parascandolo, Niki Kilbertus, Mateo Rojas-Carulla, and Bernhard Schölkopf, “Learning independent causal mechanisms,” in *Proceedings of the 35th International Conference on Machine Learning*, Jennifer Dy and Andreas Krause, Eds., Stockholmsmssan, Stockholm Sweden, 10–15 Jul 2018, vol. 80 of *Proceedings of Machine Learning Research*, pp. 4036–4044, PMLR.
- [9] N. Otsu, “A threshold selection method from gray-level histograms,” *IEEE Transactions on Systems, Man, and Cybernetics*, vol. 9, no. 1, pp. 62–66, Jan 1979.
- [10] D. Sculley, “Web-scale k-means clustering,” in *Proceedings of the 19th International Conference on World Wide Web*, New York, NY, USA, 2010, WWW 10, p. 11771178, Association for Computing Machinery.

- [11] Yue Wang, Yongbin Sun, Ziwei Liu, Sanjay E. Sarma, Michael M. Bronstein, and Justin M. Solomon, “Dynamic graph cnn for learning on point clouds,” *ACM Trans. Graph.*, vol. 38, no. 5, pp. 146:1–146:12, Oct. 2019.
- [12] Florina Piroi, Mihai Lupu, Allan Hanbury, and Veronika Zenz, “Clef-ip 2011: Retrieval in the intellectual property domain,” in *CLEF*, 2011.
- [13] Ilya Loshchilov and Frank Hutter, “SGDR: stochastic gradient descent with restarts,” *CoRR*, vol. abs/1608.03983, 2016.
- [14] Bernhard Scholkopf, “Causality for machine learning,” 2019.
- [15] K. He, X. Zhang, S. Ren, and J. Sun, “Deep residual learning for image recognition,” in *2016 IEEE Conference on Computer Vision and Pattern Recognition (CVPR)*, 2016, pp. 770–778.
- [16] Alain Hore and Djemel Ziou, “Image quality metrics: Psnr vs. ssim,” in *2010 20th International Conference on Pattern Recognition*. IEEE, 2010, pp. 2366–2369.
- [17] Han Xiao, Kashif Rasul, and Roland Vollgraf, “Fashion-mnist: a novel image dataset for benchmarking machine learning algorithms,” 2017.
- [18] Laurens van der Maaten and Geoffrey Hinton, “Visualizing data using t-sne,” *Journal of machine learning research*, vol. 9, no. Nov, pp. 2579–2605, 2008.